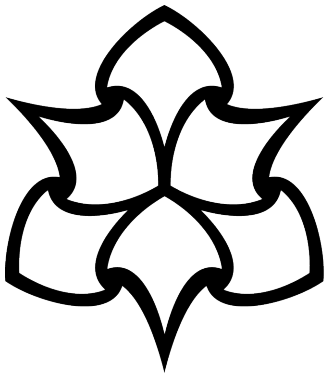

Auxetic orthotropic materials: Numerical determination of a phenomenological spline-based stored density energy and its implementation for finite element analysis.

José Crespo[a], Olly Duncan[b], Andrew Alderson[b], Francisco J. Montáns[a]

[a]*Escuela Técnica Superior de Ingeniería Aeronáutica y del Espacio*
Universidad Politécnica de Madrid
Plaza Cardenal Cisneros, 3, 28040-Madrid, Spain
[b]*Materials and Engineering Research Institute, Faculty of Science, Technology and Arts*
Sheffield Hallam University
Howard Street, Sheffield S1 1WB, United Kingdom

Abstract

Auxetic materials, which have negative Poisson's ratio, show potential to be used in many interesting applications. Finite element analysis (FEA) is an important phase in implementing auxetic materials, but may become computationally expensive because simulation often needs microscale details and a fine mesh. It is also necessary to check that topological aspects of the microscale reflects faithfully not only micro but macromechanical behaviour. This work presents a phenomenological approach to the problem using data-driven spline-based techniques to properly characterize orthotropic auxetic material requiring neither analytical constraints nor micromechanics, expanding on previous methods for isotropic materials. Hyperelastic energies of auxetic orthotropic material are determined from experimental data by solving the equilibrium differential functional equations directly, so no fitting or analytical estimation is necessary. This offers two advantages; i) it allows the FEA study of orthotropic auxetic materials without requiring micromechanics considerations, reducing modeling and computational time costs by two to three orders of magnitude; ii) it adapts the hyperelastic energies to the nature of the material with precision, which could be critical in scenarios where accuracy is essential (e.g. robotic surgery).

Keywords: Auxetic; negative Poisson's ratio; soft materials; data-driven hyperelasticity; orthotropy.

Email addresses: j.crespo@upm.es (José Crespo), o.duncan@mmu.ac.uk (Olly Duncan), a.alderson@shu.ac.uk (Andrew Alderson), fco.montans@upm.es (Francisco J. Montáns)

1. Introduction

Auxetic materials, a term first coined by Evans [1], have the property of negative Poisson's ratio. In the case of an isotropic material, the transverse section enlarges when the specimen is longitudinally stretched. In the case of an orthotropic material, Poisson's ratio varies with loading orientation. For example, it is considered that a material shows auxeticity $\nu_{xy} < 0$ during a tensile uniaxial test if, when the longitudinal strain ε_x in loading is positive, the transverse strain ε_y is also positive (instead of the negative value that a conventional material takes [2]). Initially rarely observed, such as in the case of iron pyrites [3], following the first report of man- made auxetic foam [4] multiple applications and developments have been reported [5, 6, 7, 8]. Implementation in industry [9, 10, 11, 12] requires efficient methods to predict the mechanical behavior of auxetic materials [13, 14]. If specimens undergo only small strains, a linear theory can be applied to perform the required simulations [8]. However, in many potential applications of auxetic materials, such as foam or structures for tissue engineering [15] or protective equipment [16], the auxetic material can exhibit large levels of strain. The large strains imparted in these applications often cause a nonlinear mechanical response, driven by a change in entropy of the material's micro structure [17, 18, 19].

There are different ways of characterizing and simulating complex materials such as auxetic foams. One option is an analytical phenomenological approach, which obtains an approximate solution of the stored energy density functions that defines their behavior. When these analytical functions do not give accurate predictions, some data-driven procedures may be employed both to compute material parameters [20, 21] and to select the best approximate functions/model (e.g. Bayesian methods [22, 23, 24, 25], Neural Networks [26, 27]); and for corrections for these models [28]. Once determined, data-driven material models can be implemented in FEA to perform simulations at the continuum level with reasonable modeling and computational costs. There is little prior work of this type for auxetics, and previous studies focus on isotropic auxetic foams, proposing models based on modifications of (the hyperfoam) Ogden's and the Blatz-Ko foam models [29, 30]. Because of their microstructure, many auxetic materials are anisotropic [7, 2, 31, 32, 33]. To the authors' knowledge, a continuum-based model for anisotropic auxetic foams has not been developed. Direct FEA approaches, in which a very detailed mesh considers the microstructure of the foam [34], aim to catch both the micro and macromechanical behavior, either using a very fine mesh or, more efficiently, employing Gauss-point-based multiscale approaches as e.g. FE^2 [35, 36]. Multiscale homogenization approaches are common in the simulation of hyperelastic conventional and auxetic foams; see for example [37, 38, 39, 40, 41], among others. Classical second order homogenization approaches have also been applied to conventional foams, see e.g. [42, 43], including second order (adaptive) computational homogenization approaches based on databases [44, 45]. These

typically contain the analysis of a periodic cell structure representing the foam microstructure [46, 47, 48, 49]. Some works pursue a more realistic representation of the stochastic structure of foams based on computational homogenization [50, 51]. Indeed, typical auxetic foams do not have the typical hexagonal honeycomb-like cell structure (see for example Fig. 1 in [52]). A realistic representation of the complex microstructure should be pursued in multiscale analyses, where special aspects including rib contact and changes from auxetic to conventional behavior should be considered. Then, computational homogenization approaches seem a good choice for modeling auxetic foams, but are costly for two reasons. Firstly, and most expensive, the generation of an adequate, truly Representative Volume Element (RVE) for the specific anisotropic auxetic foam is not simple, requiring specialized modelers or expensive procedures, as shown by e.g. [53]. Secondly, computational homogenization approaches are substantially more expensive in terms of computational needs (both CPU time and hardware) than continuum analysis, even though computational tasks (specially in hyperelasticity, where few state variables are present) may be alleviated by techniques including pre-computed representations (e.g. Stochastic Numerically Explicit Potentials S-NEXP [37]) and reduced models (as e.g. Proper Orthogonal Decompositions [50]). The construction of surrogate models is being pursued in several works (see e.g. [54] and therein references), where Proper Generalized Decomposition approaches (PGD) may be useful [55, 56].

Our proposed method aims to be a trade-off between the analytical phenomenological approach and the expensive full or multiscale procedures for stochastic auxetic foams. The scope of interest is modeling materials in biomechanics, medicine and other challenging disciplines where materials, such as biological tissues [57], show complex and unique properties which may not be easily accommodated with particular existing analytical stored energies. To this end, the methodology in this work follows the spline-based solution procedures which were performed successfully in isotropic conventional, isotropic auxetics, and orthotropic conventional materials [58, 59, 60]. The difficulty and specificity of application of this method to auxetic foams is caused by the different unconventional conditions that these materials can produce in the derivatives of the stored energy terms, e.g. non-injective but stable forms due to auxecticity. Herein, these conditions are studied and specific algorithms are developed to successfully solve the problem. This assumption allows to capture the high strain characteristics of orthotropic auxetic foam in all auxetic orientations.

The structure of the paper is as follows. In Sec. 2, a theoretical explanation of the orthotropic auxetic formulation is detailed, together with numerical considerations that shall be employed in the development of the methodology. For obtaining a proper solution of the mechanical behavior, we analyze valid ranges for the corresponding stored energy terms in Sec. 3. Algorithms for the data-driven methodology, developed specifically for

this material case, are explained in Sec 4. A theoretical verification and experimental validation of developed techniques are then performed in Sec 5. Finally, based on the strain energy functions determined in the previous examples, in Sec. 6, an FEA simulation is performed to study the mechanics of a sample with non-uniform geometry under high stress gradients.

2. Auxetic orthotropic hyperelastic formulation and numerical representation of stored energy terms

There are two main approaches to large strain hyperelasticity. One is based on the micromechanical behavior (e.g. chain-based models in polymers, as the Arruda-Boyce model [61]), and the other one is phenomenological. The former requires the understanding and detailed description of the physical processes involved in the specific material at the microscale [62], which thereafter is linked to the macroscale, following, for example, minimization techniques [63], an affine assumption [61], or similar micro-macro connections [64]. The latter, often referred to as the mathematical theory of nonlinear elasticity [65, 66], allows for more flexibility and adaptability to a larger scope of materials which behavior does not necessarily respond to predefined constituents and a given microstructural layout. In order to fulfill Bernstein's integrability conditions [67, 68], along with objectivity and frame-invariance from the outset, these models assume a continuum stored energy that may be defined in terms of some strain invariants. The invariants are often selected such that simplified forms (e.g. uncoupling) yield a good approximation of the experimentally observed behavior. In rubber-like materials, Mooney-Rivlin-Spencer invariants [69], or principal stretches or logarithmic strains along the Valanis-Landel uncoupling [70], are often selected. In highly compressible isotropic conventional foams, the Blatz-Ko J-invariants are a common selection [71].

Below, avoiding a microstructural description of the material (which would sacrifice a desired generality), we select a phenomenological approach employing reference logarithmic strain invariants, based on orthotropic symmetry conditions parallel to those of the infinitesimal theory.

2.1. Hyperelastic orthotropic formulation

The hyperelastic formulation aims to recover the mechanical behavior at all deformation levels. Motivated by the Valanis-Landel uncoupling, for the infinitesimal anisotropic

case, we may assume an uncoupled form

$$\Psi(\boldsymbol{\varepsilon},\ \boldsymbol{a}_1,\ \boldsymbol{a}_2) = \mathcal{U}(\varepsilon^v) + \mathcal{W}\left(\boldsymbol{\varepsilon}^d, \boldsymbol{a}_1, \boldsymbol{a}_2\right) \tag{1}$$

$$= \mathcal{U}(\varepsilon^v) + \omega_{11}\left(\varepsilon^d_{11}\right) + \omega_{22}\left(\varepsilon^d_{22}\right) + \omega_{33}\left(\varepsilon^d_{33}\right) + 2\omega_{12}\left(\varepsilon^d_{12}\right) + 2\omega_{13}\left(\varepsilon^d_{13}\right) + 2\omega_{23}\left(\varepsilon^d_{23}\right) \tag{2}$$

where $\boldsymbol{\varepsilon}$ is the infinitesimal deformation tensor, $\boldsymbol{\varepsilon}^d$ is the deviatoric part, $\varepsilon^v = tr(\boldsymbol{\varepsilon})$ is the dilatation, and the deviatoric *invariants* in the material preferred directions $\boldsymbol{a}_i$ (principal material directions which are perpendicular to the symmetry planes) are $\varepsilon^d_{ij} = \varepsilon_{ij} - \varepsilon^v_m = \boldsymbol{\varepsilon}^d : \boldsymbol{L}_{ij}$, where $\boldsymbol{L}_{ij} := \boldsymbol{a}_i \otimes \boldsymbol{a}_j$ are the structural tensors obtained by the dyadic (outer) product of the symmetry plane directions and $\varepsilon^v_m = \varepsilon^v/3$. Ψ is the total hyperelastic stored strain energy density function, $\mathcal{U}$ and ω_{ij} are the stored strain energy densities for volumetric and deviatoric contributions, respectively. For the small strain case, we use,

$$\mathcal{U}(\varepsilon^v) = \tfrac{1}{2}\kappa(\varepsilon^v)^2 \tag{3}$$

$$\omega(\varepsilon^d_{ij}) = \mu_{ij}(\varepsilon^d_{ij})^2 \tag{4}$$

where κ is the infinitesimal bulk modulus and the coefficients μ_{ij} are the typical shear moduli of the infinitesimal theory corresponding to contributions ε^d_{ij}. These equations explain the meaning of the stored energy terms. Since preferred directions $\boldsymbol{a}_i$ are invariant (fixed) in the reference configuration, we can write the reference logarithmic strains $\boldsymbol{E} = \ln \boldsymbol{U}$, where $\boldsymbol{U}$ is the right stretch tensor from the right polar decomposition, as (see details in [72]):

$$E^v := tr(\boldsymbol{E}) = \ln J = \int \frac{d\lambda_1}{\lambda_1} + \int \frac{d\lambda_2}{\lambda_2} + \int \frac{d\lambda_3}{\lambda_3} = \int d\varepsilon^v \tag{5}$$

$$E^d_{ij} := \boldsymbol{E}^d : \boldsymbol{L}_{ij} = \int d\varepsilon^d_{ij} = \int d\varepsilon_{ij} - \int \tfrac{1}{3} d\varepsilon^v = E_{ij} - \tfrac{1}{3}E^v \tag{6}$$

where $J = \lambda_1\lambda_2\lambda_3$ is the Jacobian of the deformation, $\lambda_k, k = 1,2,3$ are the principal stretches and $E^d_{ij} = \boldsymbol{E}^d : \boldsymbol{L}_{ij}$ are the *isochoric* logarithmic strain *invariants* ($\boldsymbol{L}_{ij}$ are structural tensors in the reference configuration). Note that in principal *strain* directions $E^d_i = \ln \lambda^d_i$ and $\boldsymbol{E}^d = \ln \boldsymbol{U}^d = \ln J^{-1/3}\boldsymbol{U}$, where $\lambda^d_i = J^{-1/3}\lambda_i$ are the principal isochoric stretches. Due to Eqs. (5)-(6), a parallelism between the infinitesimal framework and the large strains one is obtained. The parallelism with infinitesimal strains is beneficial for several practical reasons. First, since our common understanding is built on infinitesimal strains, much of it is preserved for the large strains context; i.e. at any large deformation level, an infinitesimal superposed deformation is interpreted in the same way as in the

reference configuration [72]. Furthermore, the interpretation of shear logarithmic terms is equal to that of infinitesimal deformations, and differs from quadratic deformations, resulting in an accurate measure of the physics behind simple shear deformations (refer to [72]). Second, intuitive additive operators are preserved (e.g. volumetric strains are the trace of the strain tensor and isochoric strains and deviatoric strains are identical), and push-forward and pull-back operations are performed with rotations (not changing the metric [73]). These observations are important in anisotropy and have facilitated the implementation of large strain anisotropic *multiplicative* plasticity and viscoplasticity preserving the additive structure of infinitesimal strain algorithms [74, 75, 76].

Due to to the parallelism with small strains, a large strain version of Eq. (2) can be immediately proposed, containing nonlinear scalar functions to be determined

$$\Psi\left(\boldsymbol{E},\ \boldsymbol{a}_1,\ \boldsymbol{a}_2\right) = \mathcal{U}\left(E^v\right) + \mathcal{W}\left(\boldsymbol{E}^d, \boldsymbol{a}_1, \boldsymbol{a}_2\right) \tag{7}$$

$$= \mathcal{U}\left(E^v\right) + \omega_{11}\left(E^d_{11}\right) + \omega_{22}\left(E^d_{22}\right) + \omega_{33}\left(E^d_{33}\right) + 2\omega_{12}\left(E^d_{12}\right) + 2\omega_{13}\left(E^d_{13}\right) + 2\omega_{23}\left(E^d_{23}\right) \tag{8}$$

The first derivative with respect to the referencial logarithmic strain tensor $\boldsymbol{E}$ yields the corresponding work-conjugate generalized Kirchhoff stress tensor $\boldsymbol{T}$, i.e. denoting $(\bullet)'$ as the derivative of the functions respect to their arguments

$$\frac{d\Psi}{d\boldsymbol{E}} \equiv \boldsymbol{T} = \sum_{i,j=1}^{3} \omega'_{ij}(E^d_{ij})\boldsymbol{L}^d_{ij} + \mathcal{U}'(E^v)\boldsymbol{I} \tag{9}$$

where $\boldsymbol{L}^d_{ij} = \boldsymbol{L}_{ij} : \mathbb{P}^d$, and $\mathbb{P}^d = d\boldsymbol{E}^d/d\boldsymbol{E} = \mathbb{I}^S - \frac{1}{3}\boldsymbol{I}\otimes\boldsymbol{I}$ is the deviatoric projector tensor, with $\mathbb{I}^S$ being the symmetric fourth order identity tensor and $dE^v/d\boldsymbol{E} = \boldsymbol{I}$ is the second order identity tensor. Note that $\omega''_{ij}(E^d_{ij}) =: 2\mu_{ij}(E^d_{ij})$ and $\mathcal{U}''(E^v) =: \kappa(E^v)$ may be interpreted as the incremental infinitesimal constants. Although not very used in the literature, the generalized Kirchhoff stress tensor $\boldsymbol{T}$ is the proper work-conjugate stress measure of the referential logarithmic strains $\boldsymbol{E}$ in the most general anisotropic case [77, 73]. Its in-axis components are coincident with the Kirchhoff in-axis stresses (hence the name), but out-of-axis are slightly different. For isotropic materials, $\boldsymbol{T}$ is the rotated Kirchhoff stress tensor, because pull-back and push-forward operations for this tensor are also performed with rotations (another advantage in anisotropic materials). The tangent modulus for this

stress-strain work-conjugate pair is,

$$\frac{d\boldsymbol{T}}{d\boldsymbol{E}} \equiv \frac{d^2\Psi}{d\boldsymbol{E}\otimes d\boldsymbol{E}} \equiv \mathbb{C} = \sum_{i,j=1}^{3} \omega''_{ij}(E^d_{ij})\boldsymbol{L}^d_{ij}\otimes\boldsymbol{L}^d_{ij} + \mathcal{U}''(E^v)\boldsymbol{I}\otimes\boldsymbol{I} \tag{10}$$

and conversions to any other stress-strain measure follow immediately using one-to-one mapping tensors obtained from the deformation gradient [73]. Experiments are usually performed in the preferred material directions. Then, for further reference, considering a system or experiment such that the loading is in the preferred material directions (so principal stresses, strains and material preferred directions are coincident), from Eq. (9), the following system of functional equations is obtained for the in-axis box (which contains principal stress and strain directions in this particular experimental setting),

$$T_1 = \tfrac{2}{3}\omega'_{11}(E^d_{11}) - \tfrac{1}{3}\omega'_{22}(E^d_{22}) - \tfrac{1}{3}\omega'_{33}(E^d_{33}) + \mathcal{U}'(E^v) \tag{11}$$

$$T_2 = -\tfrac{1}{3}\omega'_{11}(E^d_{11}) + \tfrac{2}{3}\omega'_{22}(E^d_{22}) - \tfrac{1}{3}\omega'_{33}(E^d_{33}) + \mathcal{U}'(E^v) \tag{12}$$

$$T_3 = -\tfrac{1}{3}\omega'_{11}(E^d_{11}) - \tfrac{1}{3}\omega'_{22}(E^d_{22}) + \tfrac{2}{3}\omega'_{33}(E^d_{33}) + \mathcal{U}'(E^v) \tag{13}$$

Once the in-axis functions are known, the determination of shear energy derivatives is straightforward just by using off-axis experimental data and the projection along the corresponding structural tensor $\boldsymbol{L}_{ij} = \boldsymbol{a}_i \otimes \boldsymbol{a}_j$. For instance, if a pure shear test is performed rotated 45° in-plane with normal vector in direction k, then in-axis functions cancel out and we have directly $\omega'_{ij}(E^{PS,d}_{ij}) = T_{PS}$, where $E^{PS,d}_{ij}$ and T_{PS} are the deviatoric projected experimental data of the pure shear for strain and stress, respectively.

2.2. Considerations for data-based manipulation of functions

In Section 2.1, considering the infinitesimal setting, and pursuing its recovery at any deformation level, we have posited the general decomposition of the stored energy. However in contrast to the usual analytical hyperelastic models, we have not restricted the form of these functions, but will determine their shape directly from experimental data without employing underlying analytical functions or classical material parameters. This gives the desired flexibility to model a wide range of materials at the continuum scale, from tests at that scale, without having to describe the microscale behavior or layout, an important aspect in the auxetic materials targeted in this work.

The goal of this method is to solve a system of functional equations that relates the experimental curves with the derivatives of the strain energy functions. A functional representation is required for the experimental data and for the stored strain energy functions. This conversion transforms a set of N pairs of discrete data $\{x_i, y_i\}$ $(i = 1, ..., N)$ into a function $y(x)$ that may be evaluated at any point in the continuous domain. For this purpose,

a piece-wise defined spline function is built from the data set. To eliminate experimental noise a smoothing treatment of the data can be considered before the final representation of the spline function. A choice to this regard is a least-squares B-spline function. The conversion of the discrete (experimental) set of points into the spline representation is denoted from now on as

$$\{x, y\} \rightsquigarrow y(x) \tag{14}$$

The function $y(x)$ is an approximation of the real function $y_r(x)$, partly because the available experimental information is limited to a discrete set of points and partly because of the choice of the format for the functional conversion (regression B-spline format in this work). However, usually the size of the data sets facilitates that the error in the approximation is several orders of magnitude lower than the usual numerical noise of experimental data and may be considered exact for engineering purposes. The inherent advantages of this numerical treatment are straightforward when either a function composition or an inverse function evaluation is required. From $\{x_i, y_i\} \rightsquigarrow y(x)$, the inverse function is simply obtained by generating the spline with the arguments swapped, i.e. $\{y_i, x_i\} \rightsquigarrow x(y)$. If we have another function $\{y_j, z_j\} \rightsquigarrow z(y)$, it is immediate to obtain the composition of functions

$$z(y(x)) := \{x_i, z(y_i)\} = \{x_i, z_i\} \rightsquigarrow \hat{z}(x) \tag{15}$$

Note that in Eq. (15) we use $z(y)$ from the set $\{y_j, z_j\}$ to resample the function at the z_i values in order to be immediately combined with the x_i and y_i values. We say then that we have the set $\{x_i, y_i, z_i\}$ *synchronized*, which allow the construction of any function as a combination of any of the variables x, y, z. See reference [60] for further information.

As a simple demonstrative example, consider a uniaxial test in material preferred direction 3 (the cross section is the symmetry plane $1-2$). Assume that functions $\omega'_{11}, \omega'_{22}$ are known. Our goal is to determine the corresponding strain relation caused by Poisson's ratio on transverse directions 1 and 2, namely the function $E^{3d}_{22}(E^{3d}_{11})$. Superindex number "3" indicates the preferred direction in which the load is applied in the test, superindex "d" indicates deviatoric part, and subindices denote the strain component. For the case of small strains, the required equation is,

$$\mu_{22}\varepsilon^{3d}_{22} = \mu_{11}\varepsilon^{3d}_{11} \tag{16}$$

and gives the solution in a straightforward manner, namely

$$\varepsilon^{3d}_{22} = \frac{\mu_{11}}{\mu_{22}}\varepsilon^{3d}_{11} \tag{17}$$

For large strains, the equivalent equation to Eq. (16) is

$$\omega'_{22}(E^{3d}_{22}) = \omega'_{11}(E^{3d}_{11}) \tag{18}$$

We can write the pursued relation $E^{3d}_{22}(E^{3d}_{11})$ in parametric representation, using t as intermediate variable

$$E^{3d}_{22} = t \tag{19}$$

$$E^{3d}_{11} = \omega'^{-1}_{11}\left(\omega'_{22}(t)\right) \tag{20}$$

where superindex "-1" denotes the inverse function evaluation. Equivalently, the same relation is obtained from $E^{3d}_{11} = t$ and $E^{3d}_{22} = \omega'^{-1}_{22}\left(\omega'_{11}(t)\right)$. Since the evaluation of the inverse function is simple using the mentioned spline-based procedure, we can build the objective function from discrete data, so that we have the large strain nonlinear equivalent to Eq. (17) as a function in spline format

$$\{t, \omega'^{-1}_{22}\left(\omega'_{11}(t)\right)\} \rightsquigarrow E^{3d}_{22}(E^{3d}_{11}) \tag{21}$$

Alternatively we can compute $\{\omega'^{-1}_{11}\left(\omega'_{22}(t)\right), t\} \rightsquigarrow E^{3d}_{22}(E^{3d}_{11})$. Of course, if both strain energy functions are non-injective, the evaluation of the inverse function might be undefined. The procedure to handle these cases will be addressed below.

3. Some auxetic orthotropic stability considerations

Auxeticity may cause negative values of the second derivative of strain energy functions. For this study, a bimodular material is considered in this section. It is defined with one linear behavior of μ_{ii} for evaluation in positive branch $\varepsilon^{id}_{ii} > 0$, and another linear behavior for negative branch evaluation, which has similarities to the small strain approach. In particular for our material, auxeticity may imply negative shear coefficients, i.e. $\mu_{ii} < 0$. However, not all the negative values are possible. Stability criteria on physical mechanical behavior suggest boundaries on the possible values of the energy second derivative. Since the present approach allows for a wide range of behaviors, in this section, some stability aspects of a bimodular linear material are covered to establish such boundaries.

Consider a uniaxial test performed to an ideal orthotropic material that shows a linear response in the tensile branch, and another different, but still linear, behavior for the compression branch. In this case, we could analytically describe the uniaxial test equilibrium equations performed in some preferred direction i as (note that parentheses are employed

here for κ and μ-function arguments)

$$T_i = 2\mu_{ii}(E^{id}_{ii})E^{id}_{ii} - 2\mu_{jj}(E^{id}_{jj})E^{id}_{jj} \tag{22}$$

$$0 = 2\mu_{jj}(E^{id}_{jj})E^{id}_{jj} - 2\mu_{kk}(E^{id}_{kk})E^{id}_{kk} \tag{23}$$

$$T_i = 3\kappa(E^{iv})E^{iv} \tag{24}$$

As in the previous section, subindices refer to the preferred direction they represent, first superindex i refers to the load direction of the performed uniaxial test, and the "d, v" letters indicate deviatoric (isochoric) and volumetric contributions. Note that μ and κ values depend on their arguments (i.e. one value for positive argument branch, and another one for the negative argument branch). A Drucker stability criterion during loading requires,

$$Y_i = \frac{dT_i}{dE^i_{ii}} > 0, \quad i = 1, 2, 3 \tag{25}$$

for both compressible and tensile branches of the uniaxial test in direction i, and Y_i represents the Young modulus in the corresponding direction. In order to perform the derivation of Eq. (25), we leave Eq. (22) in terms of E^{id}_{ii}, (note that in this equation $\mu_{ii}(\cdot), \mu_{jj}(\cdot)$ parenthesis are reserved for function arguments)

$$T_i = 2\mu_{ii}(E^{id}_{ii})E^{id}_{ii} + 2\mu_{jj}(-\nu^d_{ij}E^{id}_{ii})\nu^d_{ij}E^{id}_{ii} \tag{26}$$

Actually, Poisson-like ν^d_{ij} ratios are also dependent on E^{id}_{ii}, that is, $\nu^d_{ij}(E^{id}_{ii})$. In order to obtain $\nu^d_{ij}(E^{id}_{ii})$, and taking into account that μ and κ values are piecewise constant (i.e. the value of the constant depends on the region), derivation of Eq.(23) with respect to E^{id}_{ii} yields—no sum on repeated indices

$$\frac{d(2\mu_{jj}E^{id}_{jj})}{dE^{id}_{jj}}\frac{dE^{id}_{jj}}{dE^{id}_{ii}} = \frac{d(2\mu_{kk}E^{id}_{kk})}{dE^{id}_{kk}}\frac{dE^{id}_{kk}}{dE^{id}_{ii}} = \frac{d(2\mu_{kk}E^{id}_{kk})}{dE^{id}_{kk}}\frac{d(-E^{id}_{ii} - E^{id}_{jj})}{dE^{id}_{ii}} \tag{27}$$

$$\nu^d_{ij} = \frac{dE^{id}_{jj}}{dE^{id}_{ii}} = \frac{\mu_{kk}(E^{id}_{kk})}{\mu_{jj}(E^{id}_{jj}) + \mu_{kk}(E^{id}_{kk})} \tag{28}$$

If we explicitly state all the dependencies on the strain driving the uniaxial test E^i_{ii}

$$\nu^d_{ij}(E^{id}_{ii}) = \frac{\mu_{kk}(E^{id}_{kk}(E^{id}_{ii}))}{\mu_{jj}(E^{id}_{jj}(E^{id}_{ii})) + \mu_{kk}(E^{id}_{kk}(E^{id}_{ii}))} \tag{29}$$

we see that finding $\nu_{ij}^d(E_{ii}^{id})$ implies solving the implicit functional equation

$$\nu_{ij}^d(E_{ii}^{id}) = \frac{\mu_{kk}\left([\nu_{ij}^d(E_{ii}^{id}) - 1]E_{ii}^{id}\right)}{\mu_{jj}\left(-\nu_{ij}(E_{ii}^{id})\right) + \mu_{kk}\left([\nu_{ij}^d(E_{ii}^{id}) - 1]E_{ii}^{id}\right)} \tag{30}$$

As observed, it is not possible to find $\nu_{ij}^d(E_{ii}^{id})$ explicitly because the values of the shear coefficients μ in turn depend on $\nu_{ij}^d(E_{ii}^{id})$ themselves. In the case of large strains, the equivalent equation to Eq. (30) is

$$\frac{dE_{jj}^{id}}{dE_{ii}^{id}} = -\frac{\omega_{kk}''\left(-E_{ii}^{id} - E_{jj}^{id}(E_{ii}^{id})\right)}{\omega_{jj}''\left(E_{jj}^{id}(E_{ii}^{id})\right) + \omega_{kk}''\left(-E_{ii}^{id} - E_{jj}^{id}(E_{ii}^{id})\right)} \tag{31}$$

If the stability condition Eq. (25) is applied to the Equations (24), (26), (30), the condition for this bimodular orthotropic material is (parenthesis reserved for function dependencies)

$$\begin{aligned} Y_i &= \frac{dT_i}{dE_{ii}^i} = \frac{T_i}{E_{ii}^i} = \frac{T_i}{E_{ii}^{id} + 1/3E^v} = \frac{T_i}{E_{ii}^{id} + [9\kappa]^{-1}T_i} = \frac{1}{E_{ii}^{id}/T_i + [9\kappa]^{-1}} \\ &= \left[\left[2\mu_{ii}(E_{ii}^{id}) + 2\mu_{jj}\left(-\nu_{ij}^d(E_{ii}^{id})E_{ii}^{id}\right)\nu_{ij}^d(E_{ii}^{id})\right]^{-1} + [9\kappa]^{-1}\right]^{-1} > 0 \end{aligned} \tag{32}$$

This condition yields the following observations. As the compressibility increases, the term $[9\kappa]^{-1}$ gains importance, and the shear moduli coefficients may take negative values. On the contrary, in the limit of incompressibility, $\nu_{ij}^d = \nu_{ij}$, the Poisson ratio, $E_{ij}^d = E_{ij}$, and Eq. (32) becomes

$$Y_i(E_{ii}) = 2\mu_{ii}(E_{ii}^i) + 2\mu_{jj}\left(-\nu_{ij}(E_{ii}^i)E_{ii}^i\right)\nu_{ij}(E_{ii}^i) > 0 \tag{33}$$

Since the variables $\mu_{ii}, \mu_{jj}, \nu_{ij}$ keep a dependence with E_{ii}^i we assign the superindices "+","−" for the corresponding evaluation at $E_{ii}^i = \{+1, -1\}$ respectively. Then the condition under incompressibility reduces to

$$\mu_{ii}^{+/-} + \mu_{jj}^{+/-}\nu_{ij}^{+/-} > 0 \tag{34}$$

This implies that negative values of $\nu_{ij}^{+/-}$ facilitate that $\mu_{jj}^{+/-}$ also adopts negative values, if stability is satisfied as a whole for $i = 1, 2, 3$ in Eq. (25). Note that superindices "+/−" do not imply that the related variable is evaluated in the positive/negative branch respectively. This is true for μ_{ii} and ν_{ij} in Eq.(34), but not for μ_{jj} as observed in Eq.(33)

for its corresponding dependence.

As a conclusion, in incompressible orthotropic materials, a negative Poisson's ratio facilitates negative shear moduli coefficients, and compressibility further facilitates this. These situations can be easily found in orthotropic auxetic materials.

4. Determination of the auxetic orthotropic stored energy

In this section we develop the algorithms required to solve auxetic orthotropic configurations. The purpose of these algorithms is to find the energy derivative functions directly from experimental data using stress-strain equilibrium equations. Breakdown into components of equilibrium tensorial Eq. (9) for a uniaxial test performed in direction *i*, yields for the three preferred axial directions,

$$T_i = \tfrac{2}{3}\omega'_{ii}(E^{id}_{ii}) - \tfrac{1}{3}\omega'_{jj}(E^{id}_{jj}) - \tfrac{1}{3}\omega'_{kk}(E^{id}_{kk}) + \mathcal{U}'(E^{iv}) \tag{35}$$

$$0 = -\tfrac{1}{3}\omega'_{ii}(E^{id}_{ii}) + \tfrac{2}{3}\omega'_{jj}(E^{id}_{jj}) - \tfrac{1}{3}\omega'_{kk}(E^{id}_{kk}) + \mathcal{U}'(E^{iv}) \tag{36}$$

$$0 = -\tfrac{1}{3}\omega'_{ii}(E^{id}_{ii}) - \tfrac{1}{3}\omega'_{jj}(E^{id}_{jj}) + \tfrac{2}{3}\omega'_{kk}(E^{id}_{kk}) + \mathcal{U}'(E^{iv}) \tag{37}$$

After algebraic manipulation, we obtain the functional equations

$$\text{Eq. (35)} - \text{Eq. (36)} \quad \Rightarrow \quad T_i = \omega'_{ii}(E^{id}_{ii}) - \omega'_{jj}(E^{id}_{jj}) \tag{38}$$

$$\text{Eq. (36)} - \text{Eq. (37)} \quad \Rightarrow \quad \omega'_{jj}(E^{id}_{jj}) = \omega'_{kk}(E^{id}_{kk}) \tag{39}$$

$$\text{Eq. (35)} + \text{Eq. (36)} + \text{Eq. (37)} \quad \Rightarrow \quad T_i = 3\mathcal{U}'(E^{v}) \tag{40}$$

The presented algorithms are based on function refresh schemes [60]. The main purpose of the algorithms presented in this work is to compute the axial strain energy derivative functions for auxetic foams. A possible algorithm employs only experimental stress-strain data in the load direction, with the load directions being the three preferred directions. That is, it employs data $T_i(E^{id}_{ii})$ for the three $i = 1, 2, 3$ preferred directions. Using $E^d_{ii} + E^d_{jj} + E^d_{kk} = 0$ ($i \neq j \neq k \neq i$), one functional refresh algorithm could be,

$$\left\{E^{id}_{ii}\ ,\ T_i(E^{id}_{ii}) + \omega'_{jj}(E^{id}_{jj}(E^{id}_{ii}))\right\} \overset{(38)}{\rightsquigarrow} \omega'_{ii}(E^{id}_{ii}) \tag{41}$$

$$\left\{-\omega'^{-1}_{jj}\left(\omega'_{kk}(E^{id}_{kk})\right) - E^{id}_{kk}\ ,\ \omega'^{-1}_{jj}\left(\omega'_{kk}(E^{id}_{kk})\right)\right\} \overset{(39)}{\rightsquigarrow} E^{id}_{jj}(E^{id}_{ii}) \tag{42}$$

for $i = 1, 2, 3$ and corresponding indices j and k obtained by permutation. Note that in Eq. (41) the function $\omega'_{ii}(E^{id}_{ii})$ is obtained by evaluating the known functions at sampled values of E^{id}_{ii}. We say here that E^{id}_{ii} is the *running* variable. The same happens in Eq. (42)

with E^{id}_{kk} as the running variable. The running variables of the same experimental set are synchronized, (i.e. $\{E^{id}_{ii}, E^{id}_{jj}, E^{id}_{kk}\} = \{E^{id}_{ii}, E^{id}_{jj}(E^{id}_{ii}), -E^{id}_{ii} - E^{id}_{jj}(E^{id}_{ii})\}$, because this way it is not necessary to perform any interpolation to obtain E_{jj} in Eq. (41). The function $E^{id}_{jj}(E^{id}_{ii})$ has been directly obtained with the synchronized value of E^{id}_{kk} in Eq.(42).

Some additional development is needed to include orthotropic auxeticity, due to the stability conditions already explained in section 3. The functions $\omega'_{ii}(E^{id}_{ii})$ may adopt non-injective forms, and negative slopes for negative values of the strain function argument. This implies that the strain relation may not always be found even when the energy derivative functions are known. For instance, if $\omega'_{jj}(E^{d}_{jj})$ turns out to be non-injective, then the following evaluation is undefined, $E^{id}_{jj} = \omega'^{-1}_{jj}(\omega'_{kk}(E^{id}_{kk}))$. If the other involved function is injective, we can still find the relation directly through $E^{id}_{kk} = \omega'^{-1}_{kk}(\omega'_{jj}(E^{id}_{jj}))$. However, this is not always desirable because these evaluations may incur extrapolation (the functions are defined spline-wise in a finite domain). There is a general solution that avoids these difficulties, which uses the extension of Eqs. (27)-(30) to large strains. To facilitate the notation, define $x := E^{id}_{ii}$ and the function $R(x) := E^{id}_{jj}(E^{id}_{ii})$. Then, the functional equation to be solved is,

$$R(x) = \int_{x_{min}}^{x_{max}} -\frac{\omega''_{kk}\left(-x - R(x)\right)}{\omega''_{jj}\left(R(x)\right) + \omega''_{kk}\left(-x - R(x)\right)} dx \tag{43}$$

which can be solved via functional refresh method as

$$R^{[N]}(x) = \int_{x_{min}}^{x_{max}} -\frac{\omega''_{kk}\left(-x - R^{[N-1]}(x)\right)}{\omega''_{jj}\left(R^{[N-1]}(x)\right) + \omega''_{kk}\left(-x - R^{[N-1]}(x)\right)} dx \tag{44}$$

where the spline format and domain synchronizations simplify all these operations. Superindices inside square brackets $[N]$ and $[N-1]$ refer to the corresponding iteration. For the initial iteration (i.e. $R^{[0]}(x)$) either the zero function or the isotropic incompressible relation may be used, that is, $R^{[0]}(x) = 0$ or $R^{[0]}(x) = -\frac{1}{2}x$ respectively.

Finally, taking into account the discussed aspects, we detail here two functional refresh algorithms for determining deviatoric energy functions of auxetic materials from available experimental data. Algorithm 1 requires the following input data: $T_1(E^1_{11})$, stress of uniaxial test in load direction 1 versus strain in load direction 1; $E^1_{22}(E^1_{11})$, transverse strain in direction 2 versus strain in load direction 1; $E^1_{33}(E^1_{11})$, transverse strain in direction 3 versus strain in load direction 1; $T_2(E^2_{22})$ stress of uniaxial test in load direction 2 versus strain in load direction 2. An alternative algorithm is Algorithm 2, which requires instead the data $T_1(E^1_{11}), E^1_{22}(E^1_{11}), T_2(E^2_{22}), T_3(E^3_{33})$.

Algorithm 1 Available experimental data: $T_1(E^1_{11}), E^1_{22}(E^1_{11}), E^1_{33}(E^1_{11}), T_2(E^2_{22})$

1: **for** Initial guess: $\{i, j\} = \{1, 2\}, \{2, 3\}, \{3, 1\}$ **do**

$$\omega'^{[0]}_{ii}(E^d_{ii}) = 0 \tag{45}$$
$$E^{id}_{jj}(E^{id}_{ii}) = -\tfrac{1}{2}E^{id}_{ii} \tag{46}$$

2: **end for**

3: Synchronize experimental data of test 1

$$\{E^1_{11}, E^1_{22}, E^1_{33}, T_1\} = \{E^{1*}_{11}, E^1_{22}(E^{1*}_{11}), E^{1d}_{33}(E^{1*}_{11}), T_1(E^{1*}_{11})\} \tag{47}$$

4: Compute synchronized volumetric and deviatoric strains of set 1, and volumetric strain function $\mathcal{U}'(E^v)$,

$$E^{1v} = E^1_{11} + E^1_{22} + E^1_{33} \tag{48}$$
$$E^{1d}_{ii} = E^1_{ii} - \tfrac{1}{3}E^{1v} \tag{49}$$
$$\left\{E^{1v}\ ,\ T_1\right\} \rightsquigarrow \mathcal{U}'(E^v) \tag{50}$$

5: Compute synchronized volumetric and axial deviatoric strains of test 2

$$E^{2v} = \mathcal{U}'^{-1}(T_2/3) \tag{51}$$
$$E^{2d}_{22} = E^2_{22} - \tfrac{1}{3}E^{2v} \tag{52}$$

6: **while** not convergence of axial deviatoric energy functions $\omega'_{ii}(E^d_{ii})$ **do**

7: Refresh $\omega'_{11}(E_{11})$ using synchronized values of set 1 and previous function $\omega'^{[N-1]}_{22}$

$$\left\{E^{1d}_{11}\ ,\ T_1 + \omega'^{[N-1]}_{22}(E^{1d}_{22})\right\} \rightsquigarrow \omega'^{[N]}_{11}(E^d_{11}) \tag{53}$$

8: Refresh $E^{2d}_{33}(E^{2d}_{22})$ via Eq.(44), with $R(x) := E^{2d}_{33}(E^{2d}_{22})$, and $\{i, j, k\} = \{2, 3, 1\}$.

9: Refresh $\omega'_{22}(E_{22})$ using synchronized values of set 2 and previous function $\omega'^{[N-1]}_{33}$

$$\left\{E^{2d}_{22}\ ,\ T_2 + \omega^{[N-1]}_{33}(E^{2d}_{33})\right\} \rightsquigarrow \omega'^{[N]}_{22}(E^d_{22}) \tag{54}$$

10: Refresh $\omega'_{33}(E_{33})$ using synchronized values of set 1 and updated function $\omega'^{[N]}_{22}$

$$\left\{E^{1d}_{33}\ ,\ \omega'^{[N]}_{22}(E^{1d}_{22})\right\} \rightsquigarrow \omega'^{[N]}_{33}(E^d_{33}) \tag{55}$$

11: **end while**

Algorithm 2 Available experimental data: $T_1(E^1_{11}), E^1_{22}(E^1_{11}), T_2(E^2_{22}), T_3(E^3_{33})$

for Initial guess: $\{i, j\} = \{1, 2\}, \{2, 3\}, \{3, 1\}$ **do**

$$\{E^i_{ii}, T_i\} \rightsquigarrow \omega'^{[0]}_{ii} \tag{56}$$

$$E^{id}_{jj}(E^{id}_{ii}) = -\tfrac{1}{2}E^{id}_{ii} \tag{57}$$

end for

while not convergence of $\omega'_{11}(E^d_{11}), \omega'_{22}(E^d_{22}), \omega'_{33}(E^d_{33})$ **do**

Refresh $E^{1d}_{22}(E^{1d}_{11})$ via Eq.(44), with $R(x) := E^{1d}_{22}(E^{1d}_{11})$, and $\{j, k\} = \{2, 3\}$.

Find best synchronized range of E^{1v} via Eq.(58) or Eq.(59), with definitions $R^d(x) := E^{1d}_{22}(E^{1d}_{11})$, $R(x) := E^1_{22}(E^1_{11})$,

$$R(E^{1d}_{11} + \tfrac{1}{3}E^{1v}) = R^d(E^{1d}_{11}) + \tfrac{1}{3}E^{1v} \tag{58}$$

$$R^d(E^1_{11} - \tfrac{1}{3}E^{1v}) = R(E^1_{11}) - \tfrac{1}{3}E^{1v} \tag{59}$$

Synchronize the complete set of test 1, $\{E^1_{11}, E^1_{22}, E^1_{33}, E^{1v}, E^{1d}_{11}, E^{1d}_{22}, E^{1d}_{33}, T_1\}$.

Refresh $\mathcal{U}'^{[N]}(E^v) : \{E^{1v}, T_1\} \rightsquigarrow \mathcal{U}'^{[N]}(E^v)$.

Refresh $\omega'^{[N]}_{11}(E^d_{11}) : \{E^{1d}_{11}, T_1 + \omega'^{[N-1]}_{22}(E^{1d}_{22})\} \rightsquigarrow \omega'^{[N]}_{11}(E^d_{11})$

for $\{i, j, k\} = \{2, 3, 1\}, \{3, 1, 2\}$ **do**

Refresh $E^{id}_{jj}(E^{id}_{ii})$ from $\omega'^{[N-1]}_{jj}(E^d_{jj}), \omega'^{[N-1]}_{kk}(E^d_{kk})$ via Eq.(44).

Refresh $\omega'^{[N]}_{ii}(E^d_{ii}) : \{E^{id}_{ii}, T_i + \omega'^{[N]}_{jj}(E^{id}_{jj})\} \rightsquigarrow \omega'^{[N]}_{ii}(E^d_{ii})$

end for

end while

5. Theoretical verification and experimental validation

Firstly, we show that the numerical spline-based stored energy functions, and the corresponding algorithms, are capable of recovering analytical models based on a similar description of the orthotropic large strain stored energy in terms of uncoupled functions of logarithmic strain invariants (which mimic, and recover the infinitesimal counterpart at all deformation levels). To this end, pseudo-experimental data are generated from virtual tests performed using theoretical prescribed energies. These tests are thereafter prescribed to the numerical procedure. We show that the spline-based reverse-engineered energies match the analytical ones numerically, and that the predicted stresses also replicate those from the analytical function.

Obviously, when considering infinitesimal deformations and the extension of the Valanis-Landel decomposition to orthotropic materials, the uncoupled representation of the stored energy function in terms of logarithmic invariants is an approximation of the material behavior. In general, the actual behavior may present coupled terms, specially at very large deformations. Different coupled terms could be included in the stored energy (e.g. employing multidimensional splines), and these may be determined from a full set of data (including all possible loading modes and their combination up to large strains) in a purely data-driven approach. We are simply omitting them because their determination would require a large amount of tests and the procedure would be substantially more complex: note that since we are solving for the stored energy, not for stresses, we need to account for the equilibrium equations of each test in the function determination process. Since our approach is capable of exactly (i.e. to any desired precision) capturing the set of experimental data presented to the model, using additional tests we are also able to quantify the *assumption error* associated to the specific uncoupling in terms of logarithmic invariants (i.e. the actual relevance of neglected coupling terms). In our case, we will use four independent experimental curves to solve four functional unknowns, so the residual of the errors when recovering the reference experimental curves is a numerical zero. Now, if we use two extra independent test curves not employed for the energy determination, and we try to reproduce them using our obtained energies, we can assess the differences between our model and the reality (assumption error) to determine the accuracy of the assumptions.

5.1. Verification of the procedure

As a reference energy derivative function for this verification we can choose any analytical function as long as it results in stable behavior. A simple polynomial form is used

for a verification of the computational procedure

$$f(x) = \sum_{n=0}^{4} c_n x^n \tag{60}$$

This function is employed to define the (theoretical, assumed unknown) energy derivative functions, with coefficients c_n detailed in Table 1 for the argument ranges $\omega'_{11}([-0.10, 0.08])$, $\omega'_{22}([-0.12, 0.10])$, $\omega'_{33}([-0.10, 0.08])$, $\mathcal{U}'([-0.23, 0.20])$.

f	c_4	c_3	c_2	c_1	c_0
ω'_{11}	$-1.2756E+04$	$3.0974E+03$	$-1.5733E+02$	$6.0070E+01$	$4.5525E-02$
ω'_{22}	$-1.9285E+03$	$2.9568E+02$	$3.9730E+01$	$7.9928E+00$	$2.4412E-02$
ω'_{33}	$-7.7979E+03$	$-8.8494E+02$	$6.0190E+01$	$3.7911E+01$	$5.1855E-02$
$\mathcal{U}'$	$-1.0592E+02$	$8.6799E+01$	$-1.1754E+01$	$8.2847E+00$	$5.2721E-03$

Table 1: Coefficients for energy derivative function characterization in the range of application

In particular, these specific coefficient configurations are based on characterization of a real specimen, detailed in the second example (see below). If we use these energy derivatives for simulating uniaxial tests in directions 1 and 2, and generate the required "experimental" functional data for Algorithm 1 (i.e. piece-wise spline functions $T_1(E^1_{11}), E^1_{22}(E^1_{11}), E^1_{33}(E^1_{11}), T_2(E^2_{22})$), we obtain the curves shown in Figure 1. Applying Algorithm 1, we solve the required functional equations to obtain a result consisting of the set of recovered energy derivatives in the piecewise spline form shown in Figure 2. Whereas the original stored energy function and the recovered ones have obviously different analytical expressions, it is seen in this figure that they visually match. Indeed, note that cubic splines have fourth order convergence with progressive refinement, so few pieces are needed to obtain a high precision.

5.2. Experimental validation

When analyzing a real material, we have no available reference energy functions to check the goodness of the obtained ones using our procedure. However, we can determine the energy derivative functions from experimental stress-strain data obtained from some experiments, and then use these energies to simulate the tests and compare the resultant stress-strain curves with the experimental ones. Since the above-presented algorithms are developed to analyze the behavior of auxetic foams, to this end we employ experimental data from a real auxetic polyurethane foam.

The fabrication of the specimen is briefly described. First, the open cell polyurethane foam (PUR30FR, Custom Foams) was compressed using a $2mm$ walled aluminum box

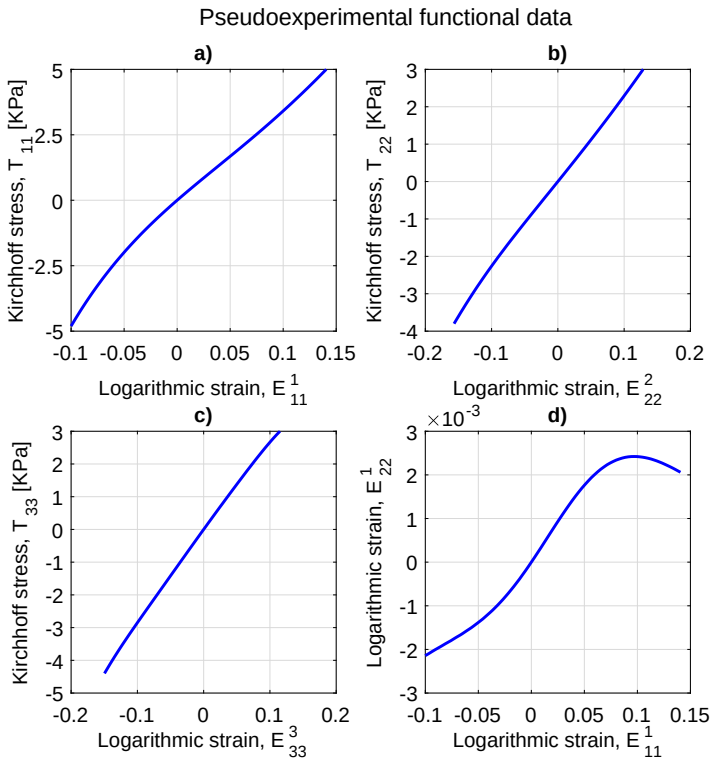

Figure 1: Pseudo-experimental test produced from reference energy derivative functions. a) Complete uniaxial test (compressible and tensile branches) performed on preferred direction 1: Kirchhoff stress vs. longitudinal logarithmic strain in load direction, $T_1(E^1_{11})$. b) Idem on preferred direction 2, $T_2(E^2_{22})$. c) Idem on preferred direction 3, $T_3(E^3_{33})$. d) Logarithmic strain relation over the uniaxial test performed on preferred direction 1: transverse logarithmic strain vs. longitudinal logarithmic strain, $E^1_{22}(E^1_{11})$. Superindices indicate preferred direction along with the test is performed.

section mold. The foam and mold were heated in an oven (MCP Tooling Technologies LC/CD) at 170°C for 20 minutes, then removed from the oven and cooled to room temperature. According to Duncan et. al. [78], at 160°C the foam presents the most negative value of the Poisson's ratio. However, temperatures above this point reduce expansion of the specimen after thermal treatment, better preserving the imposed cell structure. The final product is shown in Figure 3. The specimens were glued to end tabs to be gripped by the machine for tension-compression tests. The strain rates of the tests were $0.014 \pm 0.002 s^{-1}$. Cubic samples were selected to allow compression and tensile tests of the same sample. Although end effects may cause some error in measurement of characteristics, the purpose of the present work is to show the methodology, not to perform an accurate experimental characterization of these foams, which would require several tests on different specimens

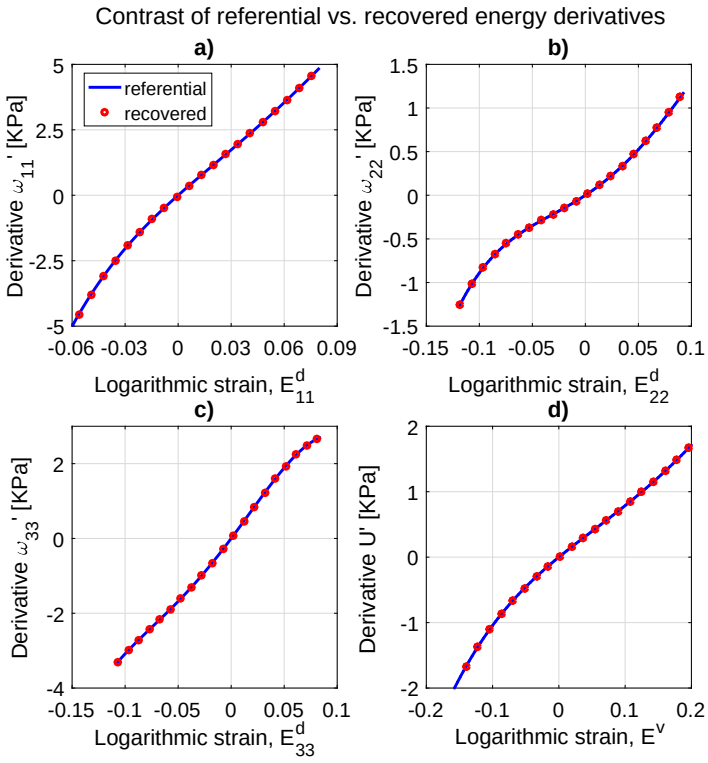

Figure 2: Comparison of reference vs. recovered energy derivative functions. a) $\omega'_{11}(E^d_{11})$, b) $\omega'_{22}(E^d_{22})$, c) $\omega'_{33}(E^d_{33})$, d) $\mathcal{U}'(E^v)$. E^d_{ii}: deviatoric logarithmic strain in preferred direction i. E^v: volumetric logarithmic strain.

and an averaging of results.

The stress-strain data were collected via Instron machine model 3369, 500N load cell and sample frequency of 25Hz. Strain data were measured using digital image correlation. A single camera Imager M-Lite with 5 Mega-pixel resolution was used, together with the AF MICRO NIKKOR lens with 60 mm optical zoom recording at 25 FPS. Figure 4 shows the experimental set up.

After smoothing to eliminate experimental noise and appropriate treatment of experimental data, we had six reference spline functions representing the experimental data sets. Since we solve four functional equations, we know that we need a minimum of four independent experimental functions; more curves could be used to obtain an average behavior. For this example we use the set $T_1(E^1_{11})$, $T_2(E^2_{22})$, $T_3(E^3_{33})$, $E^1_{22}(E^1_{11})$ to characterize the material and we use the two additional curves to check the error from the assumption of uncoupled deviatoric orthotropic contribution plus isotropic volumetric part.

Figure 5 shows some iterations and the convergence process of the energy derivative

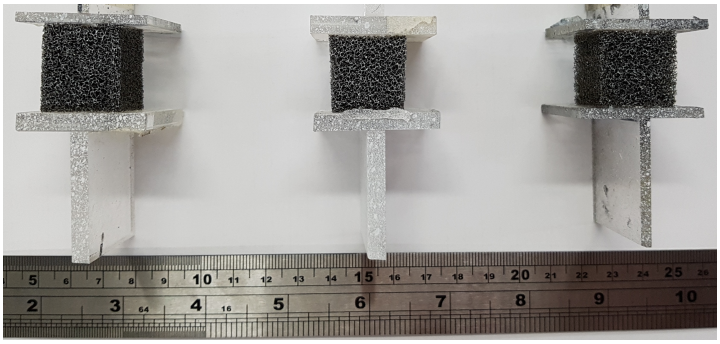

Figure 3: From left to right, samples for compressive and tensile uniaxial test for directions x, y and z

functions using the procedure described in Algorithm 2, until the system of functional equations is finally solved.

Figure 6 compares reference and simulated test curves. As observed in Figs. 6a-d the input experimental data are fully recovered. It is noticeable that extra curves Fig. 6e and Fig. 6f are not recovered. This is because they are not part of the functional system of equations to be solved. However they provide information about how close we are from the assumption of uncoupled orthotropic deviatoric and isotropic volumetric contribution of the specimen.

The assumption of uncoupled orthotropic deviatoric and isotropic volumetric contributions is seen to be reasonably accurate for $E^3_{11}(E^3_{33})$ in Fig. 6f, but less so for $E^2_{33}(E^2_{22})$ Fig. 6e. An accurate assessment of the reasons behind the discrepancies shown in Figure 6e, despite the accuracy shown in Figure 6f for the other plane, would need the microstructural insight given by multiscale analyses, with a proper description of the auxetic cell topologies and their evolution during deformation. However, the following phenomenological explanation can also be devised. Like other models in the literature, our model considers uncoupled volumetric behavior. The volumetric behavior has been determined from the curves for auxetic behavior. This means that the Poisson's ratio is negative, see e.g. Fig. 6d. Figure 6f corresponding to the $E^3_{11}(E^3_{33})$ behavior also presents auxetic behavior, so it is predicted with good accuracy even though this curve has not been used in the material characterization. However, due to the specific manufacturing process of the auxetic foam, the behavior $E^2_{33}(E^2_{22})$ shown in Figure 6e is conventional (non-auxetic, meaning that an increment in E^2_{22} produces a decrease of E^2_{33}). In this case the volumetric function, which has been characterized for auxetic behavior, is not capable of accurately predicting the completely opposite Poisson behavior present in this axis, even though it is still capable of showing a conventional behavior compatible with the prescribed curves. Of course, the inclusion of different coupled terms could improve this prediction, so a simple procedure

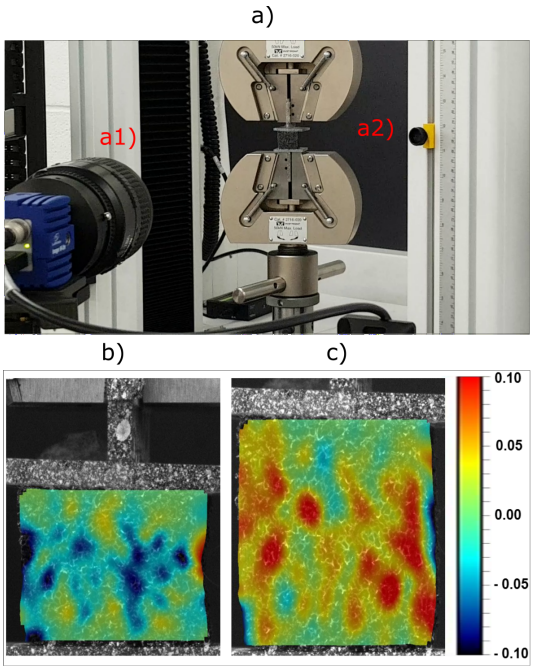

Figure 4: Test set-up. a1) Camera for digital image correlation. a2) Instron machine for compressive and tensile uniaxial test. b) Contour plot of transverse strain at maximum compression, c) Contour plot of transverse strain at maximum tension. Legend shows strain in b) and c).

of this kind that captures simultaneously auxetic and conventional behaviors with high accuracy would be valuable and is a topic of ongoing research.

Since the energies are the solution for the curves employed in the determination of the stored energy, namely Figs. 6a-d, we can assess the accuracy of the assumptions using Figs. 6e-f. We propose a *parameter of assumption error* ρ, the cumulative (integral area) relative error in absolute terms (i.e. positive differences) between the reproduced $y_{rep}(x)$ and the reference real $y_{ref}(x)$ test curves (see Fig. 6e and Fig. 6f), that is,

$$\rho(E) = \frac{1}{2E}\int_{-E}^{E}\left|\frac{y_{rec}(x) - y_{ref}(x)}{y_{ref}(x)}\right|dx \tag{61}$$

where E is the logarithmic strain limit in the abscissae of the curves that defines the range of assessment. This criterion assesses the error of continuous functions in a similar way that the statistical R^2 measure applies to discrete values. The meaning of the ρ values is intuitive, so for example the values $\rho = 0, 0.5, 1, 2$ imply respectively an error of 0%, 50% (one curve is 50% bigger than the other one), 100% (values of one curve doubles the other one) and 200% (values of one curve triples the other one). This definition computes the

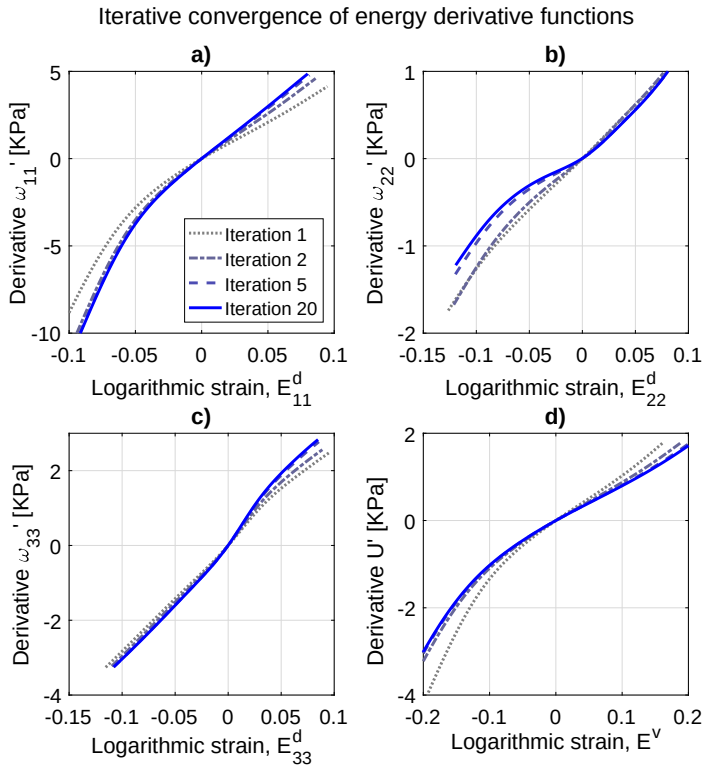

Figure 5: Iterative convergence of energy derivative functions using procedure described in algorithm 2. a) $\omega'_{11}(E^d_{11})$, b) $\omega'_{22}(E^d_{22})$, c) $\omega'_{33}(E^d_{33})$, d) $\mathcal{U}'(E^v)$. Input functional data are the complete (both compressive and tensile branches) stress-strain curves from the uniaxial tests $T_1(E^1_{11}), T_2(E^2_{22}), T_3(E^3_{33})$, and the transverse strain vs. longitudinal strain data from the uniaxial test performed in preferred direction 1, $E^1_{22}(E^1_{11})$.

relative error. Absolute positive values are also considered because errors are cumulative. Since the obtained area increases with the strain range E, the result must be divided by the range of assessment, $2E$. The proposed approach is to complete the set of uniaxial stress-strain and strain-strain test curves for the three orthotropic directions (i.e. the 6 test curves of Fig. 6) and to use the extra two curves not employed in solving the energies in order to compute the assumption error parameter using Eq. (61). The value of the logarithmic strain semi-range is $E = 0.1$, and the result is $\rho_e(0.1) = 8.927$ for the conventional behavior in Fig.6e and $\rho_f(0.1) = 0.1511$ for the auxetic behavior shown in Fig.6f.

6. Finite element analysis implementation example

The strength of this approach is that for FEA simulations it implies an important reduction in terms of characterization and computational times respect microstructural ap-

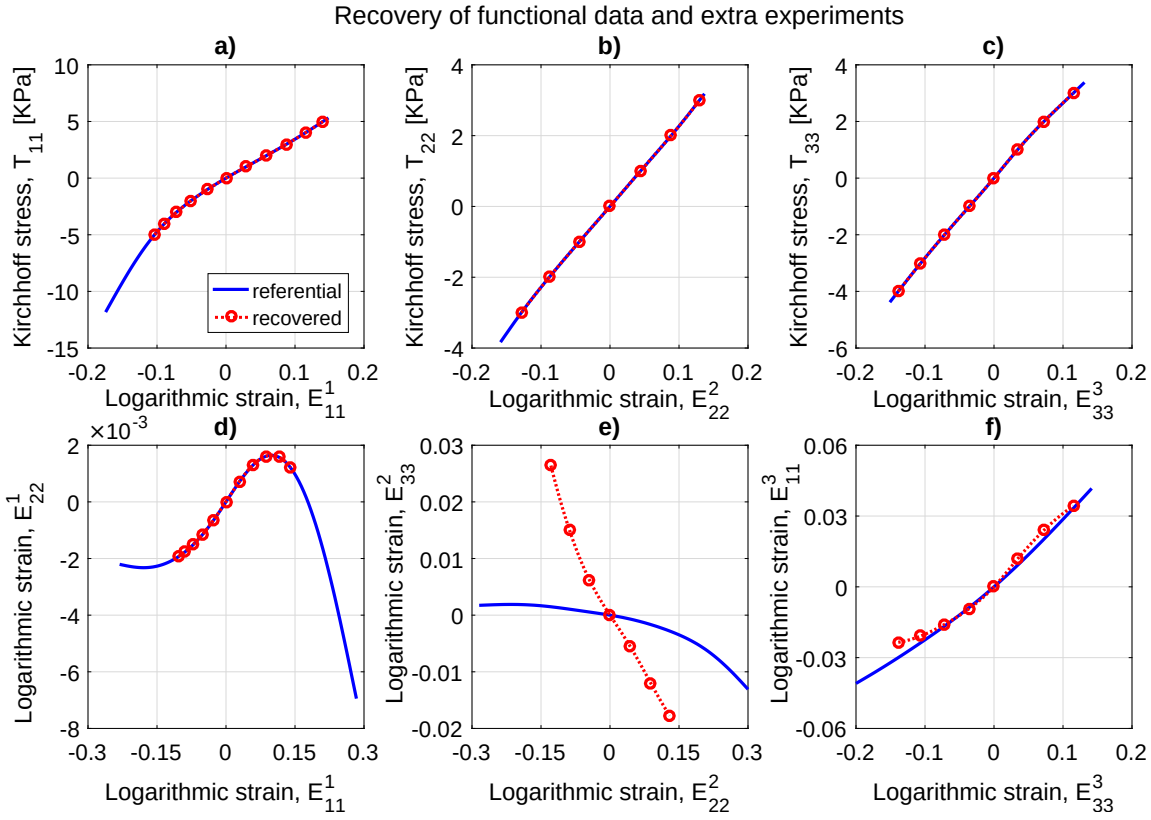

Figure 6: Recovery and contrast with reference data of original tests using combination of set of 4 functional experimental data: $T_1(E^1_{11})$,$T_2(E^2_{22})$, $T_3(E^3_{33})$, $E^1_{22}(E^1_{11})$. a) $T_1(E^1_{11})$, b) $T_2(E^2_{22})$, c)$T_3(E^3_{33})$, d) $E^1_{22}(E_{11})$, e)$E^2_{33}(E^2_{22})$, f) $E^3_{11}(E^3_{33})$. Recovery data describes a continuous function and "$\circ$" symbol in dashed lines just contributes to a better readibility

proaches. For this purpose, we present an example of FEA of an orthotropic auxetic foam. With this example we show that the spline format of the derivative energy functions can be implemented as efficiently as classical hyperelastic energies having analytical format. In the example we show that instead of using an analytical proposal for the volumetric part, the pressure is naturally determined for each integration point by the evaluation of the derivative of the volumetric strain energy function obtained from experimental data, $\mathcal{U}'$. This is possible because the function $\mathcal{U}'$ is part of the solution of the functional equations of the stress-strain equilibrium, enabling the method to recover naturally quasi-incompressible cases if data corresponds to that of a quasi-incompressible material, an advantage already observed in the isotropic compressible formulation (see Figure 14 of Reference [58]).

Energy derivative functions are based on experimental results performed on the speci-

men of the previous section, as shown in Figure 5. The evaluation of the energy functions is that of a cubic spline for interpolation and linear for extrapolation (i.e. outside the domain in which they have been determined from experimental data). In order to complete the model for our example, we take the positive branch of the defined $\omega'_{11}(E^d_{11})$ for shear energy derivatives, that is $\omega'_{12}(E^d_{12}) = \omega'_{13}(E^d_{13}) = \omega'_{23}(E^d_{23}) = \omega'^{+}_{11}(E^{+d}_{11})$. The geometry to be modeled has sharp corners and a pierced square hole in its center. In this way we can assess the mechanical behavior in a non uniform orthotropic auxetic geometry with high gradients expected. The mesh shown in Figure 7 contains $17,280$ brick elements. This choice obeys a criterium of mesh convergence and computational costs. For this simulation the computational time is 1h, 3min, 11s in a desktop PC computer running our in-house finite element program Dulcinea in a single processor and compiled with the Absoft fortran90 compiler. Global equilibrium equations have been solved using a plain Newton-Raphson method.

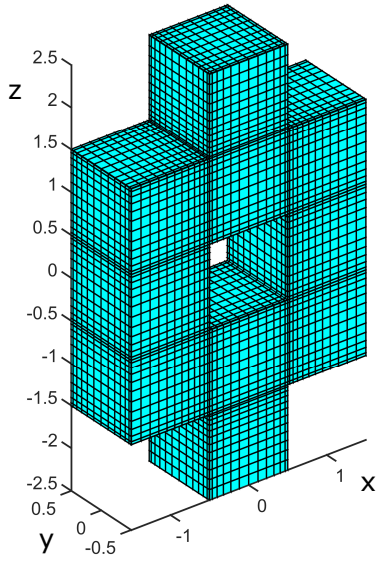

Figure 7: Geometry and mesh of the sample to be simulated for 20% stretching along the z-axis. Dimensions in mm.

The specimen is stretched to 20% of its original length. We can see the evolution of the deformation silhouette in Figure 8. We observe that the planes of symmetry must remain throughout the deformation because of the geometric and loading symmetry conditions. The load-displacement curve at the top of the specimen is shown in Figure 9. The predicted von Mises and pressure results are shown in Figure 10. High von Mises gradient is observed around the internal edges. Pressure appears more uniform along the

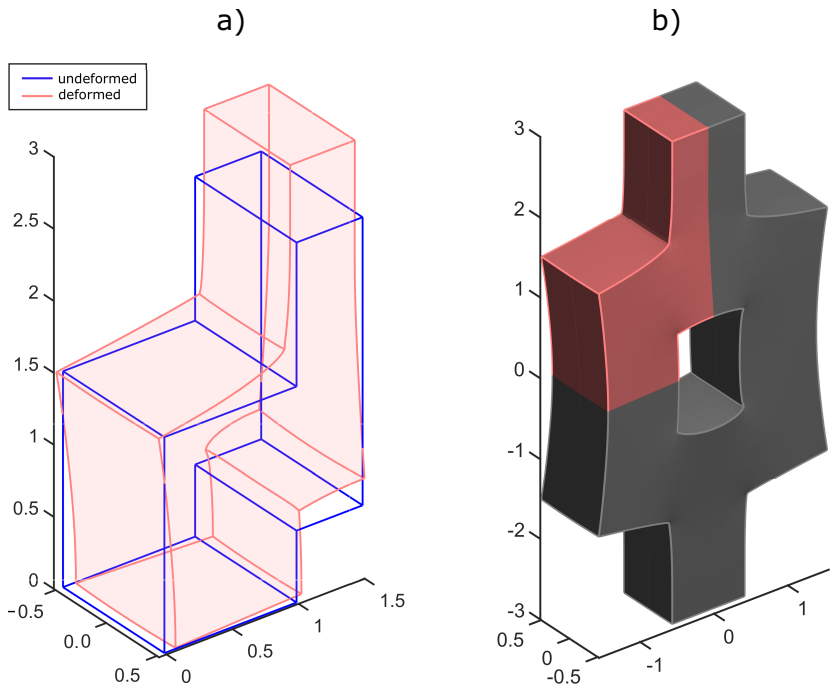

Figure 8: Deformation evolution of the sample after 20% stretching simulation. a) Detail of comparison between undeformed and deformed configurations in the upper-left quarter of the sample. In blue, relaxed configuration, initial state. In red, sample silhouette after stretching to the final state. b) Final deformation shape of the complete sample, with the upper-left quarter region detailed in "*a*)" highlighted in red.

ZX-plane sections. In order to compare computational times to problems solved using micro-macro FEA approaches we can compare to the simulations made by Tikarrouchine et. al. [36]. They used the computational homogenization FE^2 approach. Therein, they use a macroscopic mesh of only 90 elements (C3D8-Abaqus), and a microscopic one that is an RVE representing the material behavior at a point of integration of the macroscopic level. The RVE of the microscopic level contains 6857 elements (C3D4-Abaqus) at each point of integration. This simulation required 72h with 18 processors working in parallel; note furthermore that Dulcinea is a research code in which computational efficiency is not a priority (simplicity of maintenance and scientific output is prioritized), whereas Abaqus is a professional, highly optimized code. Furthermore, since they state that the parallel process was 18× faster than using a single process, their equivalent computational time is 1296h, which is more than 1000× slower than our model, which required 1.05h. Of course, other more efficient homogenization methods are available in the literature (as discussed in the Introduction Section), but undoubtedly, a continuum approach is still substantially

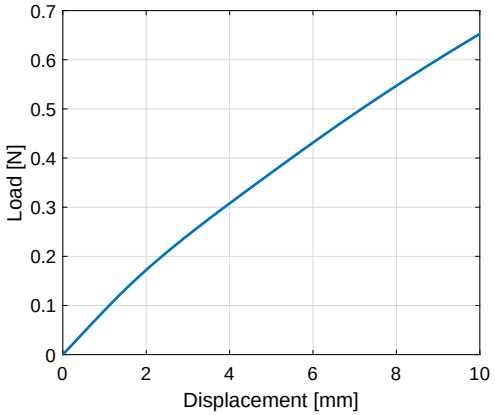

Figure 9: Load-displacement curve in the specimen (specimen stretched 20%).

more efficient for the general purpose of FEA simulation of the behavior of structures.

7. Conclusions

In this work we have developed a continuum-equivalent data-driven computational approach to model orthotropic auxetic foams in a finite element context. The approach has necessitated several developments.

First, a theoretical background to model orthotropic auxetic foams has been developed, and special conditions given by auxecticity have been addressed. The method necessitates the resolution of a system of functional equations, in which experimental tests are the functional data and the energy derivatives are the corresponding functional unknowns. The presented algorithms bypass the studied difficulties in the determination of the solution for auxetic orthotropic materials, but they also cover conventional materials.

Second, we have verified the algorithmic data-driven approach using analytical energies as a reference, showing that both the reference functions and their predictions are captured to any desired precision using the recovered spline-based energies.

Third, the experimental validation from a real specimen has been performed via uniaxial tests along with the orthotropic preferred directions. The experimental (functional) data are recovered to any desired precision. The additional test curves are employed to quantify the accuracy of the employed assumptions, which is difficult to do in analytical models due to superposition of errors, because they are difficult to separate in curves not employed in the characterization of the model. From this analysis, we observe that the model is capable of capturing auxetic behavior in orthotropic foams, but since it lacks complex coupled terms, it has difficulties in capturing simultaneously auxetic and conventional behaviors in

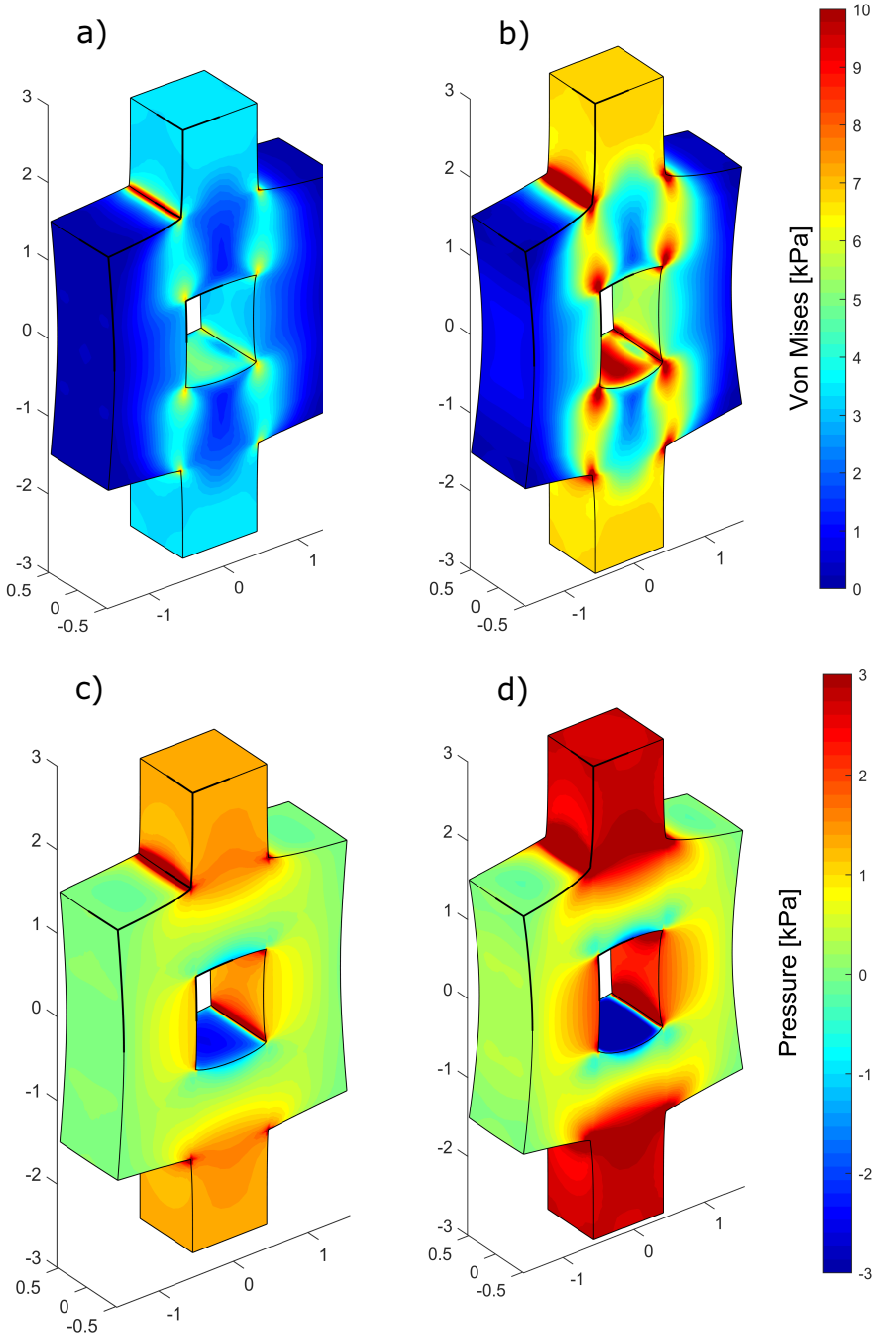

Figure 10: a) Von Mises and c) pressure [kPa] distributions after simulation of 10% stretching of the sample. b) Von Mises and d) pressure [kPa] distributions after simulation of 20% stretching of the sample. Color scales are common to both deformation levels.

different axes.

Fourth, FEA implementation of the obtained energies is performed in order to assess the computational efficiency of the method. Obtained computational times are in line with those of analytical hyperelastic models, and two or three orders of magnitude faster than multiscale analyses available in literature.

Acknowledgements

Partial financial support for this work has been given by grant PGC-2018-097257-B-C32 from the Dirección General de Proyectos de Investigación of the Ministerio de Economía y Competitividad of Spain, as well as from grant given by Universidad Politécnica de Madrid, Consejo Social, under the program called *XVII Convocatoria de ayudas del Consejo Social para el fomento de la formación y la internacionalización de Doctorandos para el curso 2018-2019*.

References

[1] K. E. Evans, M. A. Nkansah, I. J. Hutchison, S. C. Rogers (1991). Molecular Network Design. Nature, 353, 124.

[2] S. Neelakantan, W. Bosbach, J. Woodhouse, A.E. Markaki (2013). Characterization and deformation response of orthotropic fibre networks with auxetic out-of-plane behavior. Acta Materialia, 66, 326339

[3] A.E.H. Love, A Treatise on the Mathematical Theory of Elasticity, 4th ed., Dover, New York 1944

[4] R.S. Lakes (1987), Foam structures with a negative Poisson's ratio, Science, 235, 10381040.

[5] T. Allen, N. Martinello, D. Zampieri, T. Hewage, T. Senior, L. Foster, A. Alderon (2015). Auxetic foams for sport safety applications. Procedia Engineering, 112, 104-109

[6] G. E. Stavroulakis (2005). Auxetic behavior: appearance and engineering applications. Physica Status Solidi (B) Basic Research, 242(3), 710720.

[7] M. Mir, M. Najabat, J. Sami, U. Ansari (2014). Review of Mechanics and Applications of Auxetic Structures. Advances in Materials Science and Engineering. 2014-753496.

[8] K. Kumar, R.Das, E.P. Calius. (2017) 3D printable multimaterial cellular auxetics with tunable stiffness. arXiv:1707.04486

[9] Kim Alderson, Virginia Simkins (2007), US, Patent No. US7247265B2. Retrieved from https://patents.google.com/patent/US7247265B2/en.

[10] William Cass (2000), US, Patent No. US6029376A. Retrieved from https://patents.google.com/patent/US6029376A/en.

[11] David Skertchly (2010), WIPO(PCT), Patent No. WO2010026406A1. Retrieved from https://patents.google.com/patent/WO2010026406A1.

[12] Andrew Alderson, Kim Lesley Alderson, Philip John Davies, Gillian Mary Smart (2007), WIPO(PCT), Patent No. WO2007052054A1. Retrieved from https://patents.google.com/patent/WO2007052054A1.

[13] M.R. Haberman, D.T. Hook, T.D. Klatt, T.A.M. Hewage, A. Alderson, K.L. Alderson, F. Scarpa (2012). Ultrasonic characterization of polymeric composites containing auxetic inclusions. The Journal of the Acoustical Society of America, 132(3), 19611961

[14] O. Duncan, T. Allen, L. Foster, T. Senior, A. Alderson (2017). Fabrication, characterisation and modeling of uniform and gradient auxetic foam sheets. Acta Materialia, 126, 426437

[15] P. Mardling, A. Alderson, N. Jordan-Mahy, C.L. Le Maitre (2020) The use of auxetic materials in tissue engineering. Biomaterials Science, 8(8), 2074-2083.

[16] O. Duncan, T. Shepherd, C. Moroney, L. Foster, P.D. Venkatraman, K. Winwood, A. Alderson (2018). Review of auxetic materials for sports applications: Expandinf options in comfort and protection. Applied Science, 8(6), 941.

[17] J.S. Bergström. Mechanics of solid polymers: theory and computational modeling. William Andrew-Elsevier, Amsterdam, 2015.

[18] L.R.G. Treloar. The physics of rubber elasticity. Oxford University Press, Oxford, 1975

[19] I M. Ward, D.W. Hadley. An introduction to the mechanical properties of solid polymers. John Wiley & Sons Ltd., Chichester, 1993

[20] R.W. Ogden, G. Saccomandi, I. Sgura (2004). Fitting hyperelastic models to experimental data. Computational Mechanics, 34, 484-502.

[21] K. Kenja, S. Madireddy, K. Vemaganti (2020). Calibration of hyperelastic constitutive models: the role of boundary conditions, search algorithms, and experimental variability. Biomechanics and Modeling in Mechanobiology, in press. https://doi.org/10.1007/s10237-020-01318-3.

[22] K.Teferra, P. Brewick (2019). A Bayesian model calibration framework to evaluate brain tissue characterization experiments. Computer Methods in Applied Mechanics and Engineering, 357,112604.

[23] S. Madireddy, B. Sista, K. Vemaganti (2015) A Bayesian approach to selecting hyperelastic constitutive models of soft tissue. Computer Methods in Applied Mechanics and Engineering, 291, 102-122.

[24] T.G. Ritto, L.C.S. Nunes (2015). Bayesian model selection of hyperelastic models for simple and pure shear at large deformations. Computers and Structures, 156, 101-109.

[25] L.A. Mihai, T.E. Woolley, A. Goriely (2018). Stochastic isotropic hyperelastic materials: constitutive calibration and model selection. Proceedings of the Royal Society A: Mathematical, Physical and Engineering Sciences, 474,20170858

[26] Y. Shen, K. Chandrasekhara, W. Breig, L. Oliver. Neuronal network based constitutive model for rubber material (2004). Rubber Chemistry and Technology, 77, 257-277.

[27] C. Zopf, M. Kaliske (2017). Numerical characterization of uncured elastomers by a neural network. Computers and Structures, 182, 504-525.

[28] D. González, F. Chinesta, E. Cueto (2019). Learning corrections for hyperelastc models from data. Frontiers in Materials, 6, 14.

[29] J. Ciambella, G. Saccomandi (2013). A continuum hyperelastic model for auxetic materials. Proceedings of the Royal Society A 470:20130691

[30] J. Ciambella, A. Bezazi, G. Saccomandi, F. Scarpa (2015). Nonlinear elasticity of auxetic open cell foams modeled as continuum solids. Journal of Applied Physics 117, 184902.

[31] J. Dagdelen, J. Montoya, M. Jong, K. Persson (2017). Computational prediction of new auxetic materials. DOI: 10.1038/s41467-017-00399-6

[32] J.N. Grima , R. Gatt , T.G.C. Bray , A. Alderson, K.E. Evans (2005). Empirical modeling using dummy atoms (EMUDA): an alternative approach for studying auxetic structures. Molecular Simulation, 31, 915-924.

[33] J. Dirrenberger, S. Forest, D. Jeulin (2013). Effective elastic properties of auxetic microstructures: anisotropy and structural applications. International Journal Mechanics and Materials in Design, 9, 2133

[34] A.A. Javadi, A. Faramarzi, R. Farmani (2012). Design and optimization of microstructure of auxetic materials. Engineering Computations, 29(3), 260276.

[35] F. Feyel, J.L. Chaboche (2000). FE2 multiscale approach for modeling the elastoviscoplastic behavior of long fibre SiC/Ti composite materials. Computer Methods in Applied Mechanics and Engineering, 183(3-4), 309330.

[36] E. Tikarrouchine, G. Chatzigeorgiou, F. Praud, B. Piotrowski, Y. Chemisky (2018). Three-dimensional FE2 method for the simulation of non-linear, rate-dependent response of composite structures. Composite Structures, 193:165-179.

[37] A. Clément, C. Soize, J. Yvonnet (2012). Computational nonlinear stochastic homogenization using a nonconcurrent multiscale approach for hyperelastic heterogeneous microstructures analysis. International Journal for Numerical Methods in Engineering, 91,799-824.

[38] K. Gao, J.A.W. van Dommeten, M.G.D. Geers (2016). Microstructure characterization and homogenization of acoustic polyurethane foams: Measurements and simulations. International Journal of Solids and Structures 2016, 101, 536-546.

[39] V. Hardenacke, J. Hohe (2009). Local probabilistic homogenization of two-dimensional model foams accounting for micro structural disorder. International Journal of Solids and Structures, 46,989-1006

[40] A. Heydari, A. Vahidifar, E. Esmizadeh, D. Rodrigue (2020). Experimental and finite element simulation of natural rubber foams using real 3D structures. Polymer, 197, 122505

[41] J. Ju, J.D. Summers (2011). Hyperelastic constitutive modeling of hexagonal honeycombs subjected to in-plane shear loading. Journal of Engineering Materials and Technology, 133, 011005

[42] O. López-Pamies, P Ponte Castañeda (2004). Second-order estimates for the macroscopic response and loss of ellipticity in porous rubbers at large deformations. Journal of Elasticity, 76, 247-287

[43] P. Ponte-Castañeda, E. Tiberio (2000) A second order homogenization method in finite elasticity and applications to black-filled elastomers. Journal of the Mechanics and Physics of Solids, 48, 1389-1411.

[44] I. Temizer, P. Wriggers (2011). An adaptive multiscale resolution strategy for the finite deformation analysis of microheterogeneous structures. Computer Methods in Applied Mechanics and Engineering 200,2639-2661.

[45] I. Temizer, P. Wriggers (2007). An adaptative method for homogenization in orthotropic nonlinear elasticity. Computer Methods in Applied Mechanics and Engineering, 196,3409-3423.

[46] H.-G. Sehlhorst, R. Jnicke, A. Duster, E. Rank, H. Steeb, S. Diebels (2009). Numerical investigations of foam-like materials by nested high-order finite element methods. Computational Mechanics, 2009, 45:45-59.

[47] Y. Wang, A.M. Cuitiño (2000). Three-dimensional nonlinear open-cell foams with large deformations. Journal of the Mechanics and Physics of Solids, 48:, 961-988.

[48] W. Zhu, N. Blal, S. Cunsolo, D. Baillis (2017). Micromechanical modeling of effective properties of open-cell foam. International Journal of Solids and Structures, 115, 61-72.

[49] W. Zhu, N. Blal, S. Cunsolo, D. Baillis, P.-M. Michaud (2018). Effective Elastic Behavior of Irregular Closed-Cell foams. Materials, 11, 2100

[50] J. Yvonnet, Q.-C. He (2007). The reduced model multiscale method (R3M) for the non-linear homogenization of hyperelastic media at finite strains. Journal of Computational Physics, 223, 341-368.

[51] H. Zeinalabedini, Y.O. Yildiz, P. Zhang, L. Laux, M. Kirca, A.C. To (2016). Homogenization of additive manufactured polymeric foams with spherical cells. Additive Manufacturing, 12, 274-281

[52] J.N. Grima, R. Gatt, N. Ravirala, A. Alderson, K.E. Evans (2006). Negative Poisson's ratios in cellular foam materials. Materials Science and Engineering A, 423, 214-218.

[53] M.A. Bessa, R. Bostanabad, Z. Liu, A. Hu, D.W. Apley, C. Brinson, C. Chen, W.K. Liu (2017). A framework for data-driven analysis of materials under uncertainty: Countering the curse of dimensionality. Computer Methods in Applied Mechanics and Engineering, 350, 633-667.

[54] B. Staber, J. Guilleminot (2017). Functional approximation and projection of stored energy functions in computational homogenization of hyperelastic materials: A probabilistic perspective. Computer Methods in Applied Mechanics and Engineering, 313; 1-27.

[55] S. Niroomandi, I. Alfaro, D. Gonzalez, E. Cueto, F. Chinesta (2013). Model order reduction in hyperelasticity: A Proper Generalized Decomposition approach. International Journal for Numerical Methods in Engineering, 96,129-149.

[56] F. Chinesta, E. Cueto (2014). PGD-Based Modeling of Materials, Structures and Processes. Springer, doi: 10.1007/978-3-319-06182-5.

[57] C. Lees, J.F. Vincent, E. Hillerton (1991). Poisson's ratio in skin. Bio-medical Materials and Engineering 1(1):19-23

[58] J. Crespo, M. Latorre, F.J. Montáns (2017). WYPIWYG hyperelasticity for isotropic, compressible materials. Computational Mechanics, 59(1), 73-92.

[59] J. Crespo, F.J. Montáns(2017). A continuum approach for the large strain finite element analysis of auxetic materials. International Journal of Mechanical Sciences. 2017(135) pp.441-457

[60] J. Crespo, F.J. Montáns (2018). Function-refresh algorithms for determining the stored energy density of nonlinear elastic orthotropic materials directly from experimental data. International Journal of Non-Linear Mechanics. 107(2018)16-33.

[61] E. M. Arruda, M. C. Boyce (1993) A three-dimensional constitutive model for the large stratch behavior of rubber elastic materials. Journal of the Mechanics and Physics of Solids, 41(2):389-412.

[62] O. López-Pamies, R. Gracía, E. Chabert, J.-Y.Cavaillé, P. Ponte-Castañeda (2008). Multiscale modeling of oriented thermoplastic elastomers with lamellar morphology. Journal of the Mechanics and Physics of Solids, 56(11):3206-3233.

[63] P. Ponte Castañeda (1992). Bounds and estimates for the properties of nonlinear heterogeneous systems. Phil. Trans. Royal Soc. A: Math. Phys. & Engrg. Sci. 340(1659), doi: 10.1098/rsta.1992.0079

[64] V.J. Amores, J.M. Benitez, F.J. Montáns (2019). Data-driven, structure-based hyperelastic manifolds: A micro-macro-micro approach to reverse-engineer the chain behavior and perform efficient simulations of polymers. Computers and Structures, in press, arXiv:1903.11545.v2 [cond-mat.mtrl-sci].

[65] R.W. Ogden (1984). Non-Linear Elastic Deformations. Ellis Harwood, Chichester, England.

[66] J.E. Marsden, T.J.R. Hughes (1983). Mathematical Foundations of Elasticity. Prentice-Hall, New Jersey.

[67] B. Bernstein (1960). Relations between hypoelasticity and elasticity. Transactions of the Society of Rehology IV: 23-28.

[68] B. Bernstein (1960). Hypo-elasticity and elasticity. Archives of Rational Mechanical Analalysis 6(1): 89-104.

[69] R. S. Rivlin, G. I. Barenblatt, and D. D. Joseph (1997). Collected papers of RS Rivlin, volume 1. Springer Science & Business Media, New York, 1997.

[70] E. H. Twizell, R. W. Ogden (1983). Non-linear optimization of the material constants in Ogden's stress-deformation function for incompressible isotropic elastic materials. Journal of the Australian Mathematical Society B 24(04):424-434.

[71] P. J. Blatz, W. L. Ko (1962). Application of finite elastic theory to the deformation of rubbery materials. Transactions of the Society of Rheology 223-251.

[72] M. Latorre, F.J. Montáns (2014). On the interpretation of the logarithmic strain tensor in an arbitrary system of representation. International Journal of Solids and Structures 51(7-8): 1507-1515.

[73] M. Latorre, F.J. Montáns (2016). Stress and strain mapping tensors and general work-conjugacy in large strain continuum mechanics. Applied Mathematical modeling, 40 (5-6), 3938-3950.

[74] M. Latorre, F.J. Montáns (2015). Anisotropic finite strain viscoelasticity based on the Sidoroff multiplicative decomposition and logarithmc strains. Computational Mechanics, 56, 503-531.

[75] M. Latorre, F.J. Montáns (2016). Fully anisotropic finite strain viscoelasticity based on a reverse multiplicative decomposition and logarithmic strains. Computers and Structures, 163, 56-70.

[76] M.A. Sanz, F.J. Montáns, M. Latorre (2017). Computational anisotropic hardening multiplicative elastoplasticity based on the corrector elastic logarithmic strain rate. Computer Methods in Applied Mechanics and Engineering, 320, 82-121.

[77] F.J. Montáns, K.J. Bathe (2015). Towards a model for large strain anisotropic elastoplasticity. Ch. 1 in: Computational Plasticity, E. Oñate, R. Owen (eds.), Springer. 13-36.

[78] O. Duncan, F. Clegg, A. Essa, A. Bell, L. Foster, T. Allen, et al (2018). Effects of Heat Exposure and Volumetric Compression on Poissons Ratios, Youngs Moduli, and Polymeric Composition During Thermo-Mechanical Conversion of Auxetic Open Cell Polyurethane Foam. Phys Status Solidi B, 1800393.